J Mater Sci (2006) 41:7843–7852
DOI 10.1007/s10853-006-0562-1

The formation mechanism of aluminium oxide tunnel barriers

A. Cerezo · A. K. Petford-Long · D. J. Larson · S. Pinitsoontorn · E. W. Singleton

Received: 10 March 2006 / Accepted: 13 June 2006 / Published online: 24 October 2006

Abstract The functional properties of magnetic tunnel junctions are critically dependant on the nanoscale morphology of the insulating barrier (usually only a few atomic layers thick) that separates the two ferromagnetic layers. Three-dimensional atom probe analysis has been used to study the chemistry of a magnetic tunnel junction structure comprising an aluminium oxide barrier formed by in situ oxidation, both in the under-oxidised and fully oxidised states and before and after annealing. Low oxidation times result in discrete oxide islands. Further oxidation leads to a more continuous, but still non-stoichiometric, barrier with evidence that oxidation proceeds along the top of grain boundaries in the underlying CoFe layer. Post-deposition annealing leads to an increase in the barrier area, but only in the case of the fully oxidised and annealed structure is a continuous planar layer formed, which is close to the stoichiometric Al:O ratio of 2:3. These results are surprising, in that the planar layers are usually considered unstable with respect to breaking up into separate islands. Analysis of the various driving forces suggests that the formation of a continuous layer requires a combination of factors, including the strain energy resulting from the expansion of the oxide during internal oxidation on annealing.

A. Cerezo (✉) · A. K. Petford-Long · D. J. Larson · S. Pinitsoontorn
Department of Materials, University of Oxford, Parks Road, Oxford OX1 3PH, UK
e-mail: alfred.cerezo@materials.oxford.ac.uk

E. W. Singleton
Recording Head Operations, Seagate Technology, Minneapolis, MN 55435, USA

Present Address:
A. K. Petford-Long
Argonne National Laboratory, Argonne IL 60439, USA

Present Address:
D. J. Larson
Imago Scientific Instruments, Madison WI 53719, USA

Introduction

Magnetic tunnel junctions (MTJs) display tunnelling magnetoresistance (TMR) and thus have applications in a range of novel spin-electronic devices, including magnetic sensors and solid-state memory [1]. The TMR phenomenon arises because of the difference in magnitude of the spin-dependent electron tunnelling across a nanoscale insulating barrier as a function of the relative orientation of the magnetisation in two ferromagnetic layers [2, 3]. Numerous materials have been studied as candidates for the insulating barrier, including AlN [4], MgO [5] and Hf oxide [6], but the most widely used barrier material is aluminium oxide. Since it is difficult to obtain a uniform oxide layer directly by sputtering, aluminium oxide layers are formed by deposition of a thin Al layer (down to a few monolayers thick) followed by in situ oxidation using one of several methods including natural oxidation and plasma oxidation [7].

The morphology and composition of the oxide barrier and the barrier/ferromagnet interfaces play a major role in determining the properties of TMR devices. The magnitude of the spin polarisation within the

ferromagnetic layers adjacent to the tunnel barrier layer is an important factor in the TMR achieved [8], and this will be influenced by intermixing at the oxide/ferromagnet interface. Variations in the barrier width or in barrier height across the tunnel junction structure, arising because of variations in oxidation state of the Al, can lead to tunnelling only through small regions of the barrier [9, 10]. Indeed, a barrier structure with significant contacts between the FM layers (usually termed 'pinholes') might be expected not to show the characteristics of electron tunnelling. However, Rabson et al. have shown that structures with barriers containing pinholes can exhibit TMR and show the expected exponential decrease in tunnelling current with increase in barrier width [11].

Characterisation of the microstructure of tunnel barriers has been carried out using a number of techniques including high resolution electron microscopy (HREM) [12, 13], electron energy loss spectroscopy [14], X-ray techniques [15], and Fourier transform infrared spectroscopy [16]. However at these sub-nanometre thicknesses it is extremely difficult to visualise tunnel barriers experimentally and therefore the process by which the barrier is formed remains poorly understood. In the current work we have used three-dimensional atom probe (3DAP) analysis [17, 18] to analyse a simple MTJ structure with atomic resolution, in order to study the chemistry and morphology of the tunnel barrier and to elucidate the mechanisms of barrier formation. 3DAP and HREM data on the early stages of oxidation of the barrier have been presented previously [19]. In this paper we are able to add data on fully oxidised samples before annealing, and so elucidate the later stages of oxidation and subsequent annealing. Together with the previous data, which is reproduced here for convenience, we are able to provide a complete survey of the different stages of oxidation, and thus present a discussion of the mechanisms that lead to the formation of a continuous barrier in a TMR device.

Experimental details

The samples analysed were unpinned magnetic tunnel junction structures consisting of //seed/$CoFe_{6\ nm}$/$Al_{0.6\ nm}$ (oxidized)/$CoFe_{3\ nm}$/cap. The samples were grown by DC magnetron sputter deposition (base pressure ~1×10^{-7} Pa) and the substrates used were low resistivity Si (100) wafers held at approximately room temperature. The surface of the Si had been etched to provide a thin amorphous Si layer on which the seed was deposited, so as to avoid any potential problems with epitaxy on the crystalline Si wafer. The tunnel barrier was formed by in situ natural oxidation (oxygen pressure kept constant). A range of oxidation times were studied, of which two have been chosen for inclusion in this paper: that needed to produce fully oxidized barriers (1.0 t_{ox}) and a shorter time (0.25 t_{ox}) used to produce an under-oxidised barrier. The resultant structures were analysed both in the as-deposited state and after annealing at 250 °C for 4 h. Cross-sectional HREM samples were prepared from the film and examined in a JEOL 4000EX TEM with point-to-point resolution of 0.18 nm.

Samples for 3DAP analysis are in the form of sharp needle points, of approximately 50 nm end radius. The Si substrates used for preparation of 3DAP samples were patterned into posts prior to deposition [20]. After deposition and annealing, individual posts were removed from the samples and sharpened using focused ion-beam milling [21]. 3DAP analysis was performed in an energy-compensated optical position-sensitive atom probe [22] in a vacuum of ~5×10^{9} Pa, at a specimen temperature of 70–80 K. Analysis was performed using either voltage pulsing with a pulse fraction of 15% and a pulse repetition rate of 1500 Hz, or femtosecond laser pulsing with a pulse repetition rate of 10 kHz. Both voltage and laser pulsing was used to analyse the fully oxidised, annealed material and both yielded a Al:O ratio in the barrier of close to the expected 2:3 stoichiometry.

Results

The overall development in the barrier with oxidation and annealing can be seen by comparing the HREM images of the under-oxidised, as-deposited sample and the fully-oxidised, annealed sample, shown in Fig. 1. In HREM images, the oxide regions appear pale, and generally show the contrast which would be expected from an amorphous oxide, being easily distinguished from the darker metallic regions in which clear lattice fringes are visible. However, partial oxidation has resulted in the formation of a barrier region that contained significant ''pinholes'' which connect the ferromagnetic layers on either side. In places the CoFe lattice fringes extend across the barrier region, such as the area marked out in Fig. 1a, which shows the contrast expected in a sample containing both metal and oxide viewed in projection. The HREM for the fully oxidised, annealed sample, Fig. 1b shows a continuous barrier with a width of ~2 nm. Although the HREM images show the changes in microstructure and also give an indication of the extent of pinhole formation

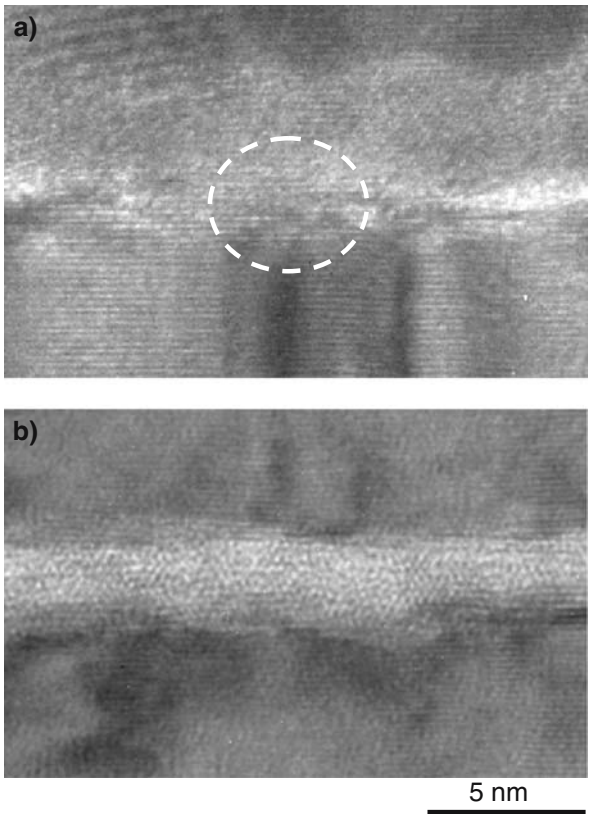

Fig. 1 HREM cross-sectional images showing the morphology of the barrier (**a**) in the under-oxidised as-deposited sample and (**b**) in the fully oxidised sample after annealing at 250 °C for 4 h. Micrographs reproduced with permission from J Appl Phys 98:124904 © 2005, American Institute of Physics

they do not give direct information about the composition in the barrier region.

Details on the 3-dimensional atomic-scale morphology of the barrier and the variations in chemistry within the oxide can be obtained from 3DAP analysis of the films. The 3DAP data in Fig. 2 are shown as isoconcentration surfaces drawn at a composition of (Al + O) = 15 at.% and therefore show the three-dimensional volumes within the data where the concentration is above this level. Also shown in Fig.2a–c are two-dimensional composition maps from a ~0.35 nm thick slice running vertically through regions of relatively high Al + O content, thus marking the approximate plane of the barrier. The Al + O concentration in this slice is represented on a greyscale, in which 0 at.% (Al + O) is shown as black and >15 at.% (Al + O) as white. The data are displayed at an angle so that the three-dimensional nature of the 3DAP data can be clearly visualised. The isosurface of Fig. 2a clearly shows that a planar barrier layer has not been formed in the under-oxidised sample, but rather that islands of oxide (high Al + O concentration) were

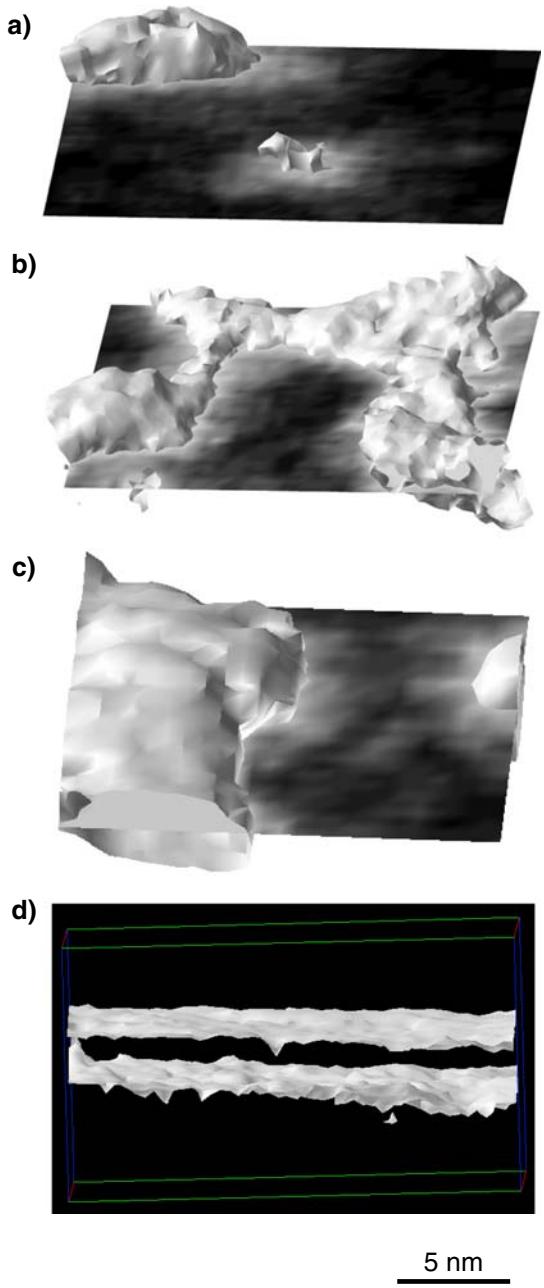

Fig. 2 3DAP isoconcentration surface reconstructions showing the morphology of the barrier in the under-oxidised sample (**a**) as deposited and (**b**) after annealing for 4 h at 250 °C, and in the fully oxidised sample (**c**) as deposited and (**d**) after annealing. (**a**), (**b**) and (**d**) reprinted with permission from J Appl Phys 98:124904, © 2005, American Institute of Physics

present. Apart from within the islands, the Al and O content within the film was low, although some slight enhancement of the Al and O level was observed along lines between the islands (seen faintly in Fig. 2a). The chemistry of the oxidised islands can be quantified in more detail by constructing composition–depth profiles through the region marked by the isoconcentration

surface, and these are shown in Fig. 3. Note that the film growth direction is from right to left in the composition profiles. It is clear that the islands observed in the under-oxidised sample are far from being stoichiometric Al_2O_3, having a considerable Co content (of the order of 25 at.%) and an Al:O ratio of ~2:1, as shown in Fig. 3a. The profile also shows clearly that the oxidised regions extend several nanometres in a direction normal to the barrier plane. The total Al content in the 3DAP data corresponds approximately to that expected for a 0.6 nm thick layer.

The effect of annealing the under-oxidised sample is shown in Figs. 2b and 3b. Following annealing the more heavily oxidised islands have extended to form a connected network across the sample, resulting in a greater area of oxide tunnel barrier. A further result of the annealing process is that the extent of the oxidised regions normal to the barrier plane has decreased, as shown in the composition profile of Fig. 3b. The composition profile also shows that the Al:O ratio in the central ~1 nm or so of barrier has not changed significantly after annealing, but that the concentration of both elements increased and that of Co decreased.

From more detailed work on other under-oxidised films, it was found that the number of oxide islands increased with increasing oxidation time [19]. The lateral and vertical (i.e. perpendicular to the barrier plane) extent of the oxide islands was also observed to increase, reaching a size that extended several nanometres in a direction normal to the barrier plane. In the fully oxidised case, the oxide is seen to have extended to the stage where it almost forms a network in the barrier plane, even before annealing, as shown in Fig. 2c). Some Al and O are observed between the extended islands, along lines that would tend to extend the network further, as seen in the composition map. However, some Al and O are observed across the whole width of the film. For example, in the area that is seen to have the least Al + O from Fig. 2c, 211 Al atoms and 154 O atoms were observed from an area 5×5 nm in the plane of the barrier, and a depth of 5 nm corresponding to the barrier position. (Al and O atoms were broadly distributed in depth at this location, rather than being confined to a narrow depth as might mark the original surface.) A composition profile through the island, Fig. 3c, shows that the chemistry of the barrier is not very different to the under-oxidised case, although there is some oxidation of the underlying Co. A significant level of Co remains (Al:Co approximately 1, as in the under-oxidised case).

Only after annealing of the fully oxidised sample is a continuous barrier layer formed, Fig. 2d, with a thickness of approximately 1 nm (full-width at half maximum of the O peak in the composition profile of

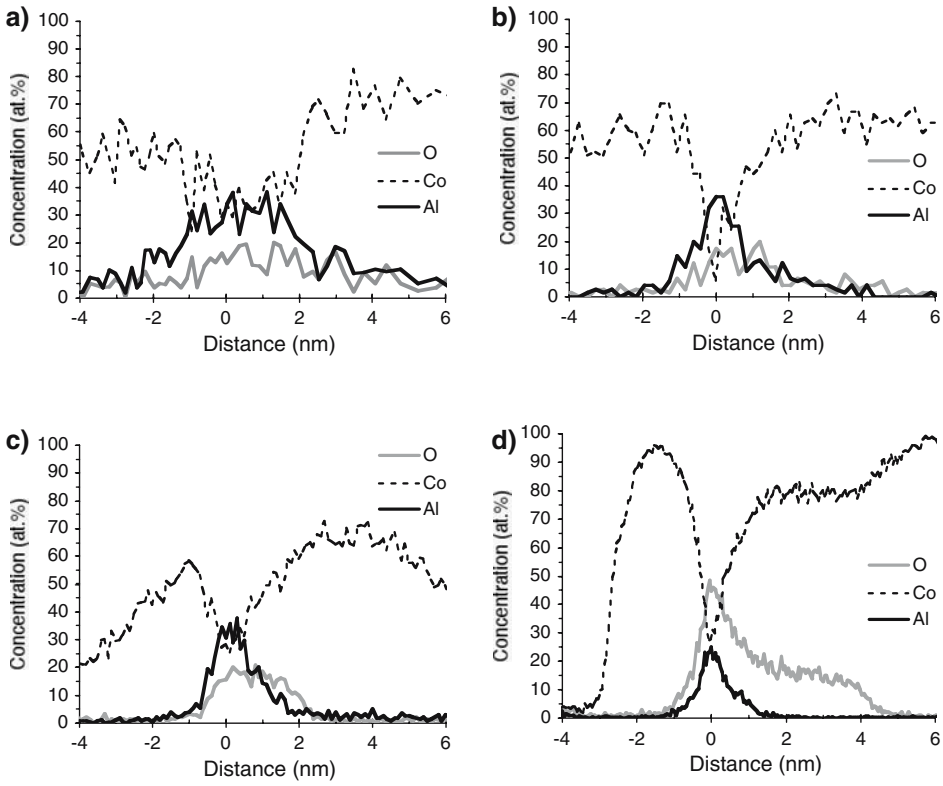

Fig. 3 Composition depth profiles across the barrier oxide from the 3DAP analysis of the under-oxidised sample (**a**) as deposited and (**b**) after annealing for 4 h at 250°C, and from the fully oxidised sample (**c**) as deposited and (**d**) after annealing. In these composition profiles, the growth direction is from right to left. (**a**), (**b**) and (**d**) redrawn with permission from J Appl Phys 98:124904, © 2005, American Institute of Physics

Fig. 3d). The Al:O ratio in the barrier was measured to be ~0.60 (i.e. close to stoichiometric Al_2O_3) although the barrier region still contains about 20 at.% Co. In addition, a long tail in the oxygen content can be seen extending ~3.5 nm into the underlying CoFe layer, with an oxygen concentration of about 17 at.%. It is interesting that the profile shows a distinct plateau in the composition: although there is no equilibrium Co oxide phase at this composition, this suggests a metastable phase formation. Some oxidation of the upper CoFe layer is also evident, with the oxygen profile rising before that of aluminium. Clearly, the Al in the barrier has acted as a getter during annealing, collecting free oxygen that was trapped in the rest of the film following the longer oxidation treatment. This gettering behaviour is well known: for example Lehnert et al. showed that the barrier in a Nb–Al/AlO_x/Nb tunnel junction increased in thickness on annealing, even when the anneal was performed in nitrogen or after a nitridation treatment that would prevent residual oxygen entering the structure [23]. In the present case, the additional oxygen allows the barrier to complete the oxidation and form a layer that is close to the expected Al:O ratio of 2:3.

Discussion

The experimental results provide clear evidence that the barrier morphology develops from one consisting of individual, isolated islands, to an interconnected network on the length scale of the grains in the underlying CoFe layer, and finally (on annealing) to a continuous layer. However, it should be remarked that this evolution from isolated particles to a layer is contrary to what would normally be expected, since a flat layer is metastable against surface energy driven spherodisation, which in a general case would drive the system towards spherical islands. Thus it is clear that even if the continuous layer that is observed after full oxidation and annealing is highly metastable, the initial state is even more metastable. What has been observed is clearly part of a rather complicated trajectory towards the final thermodynamically stable state of large isolated Al_2O_3 particles. In this section we consider the different stages of the process and the factors that lead to the formation of the planar barrier layer, which are illustrated by the schematic of Fig. 4.

Zhou and Wadley have simulated the sputter deposition of Al onto a $Ni_{65}Co_{20}Fe_{15}$ substrate, and

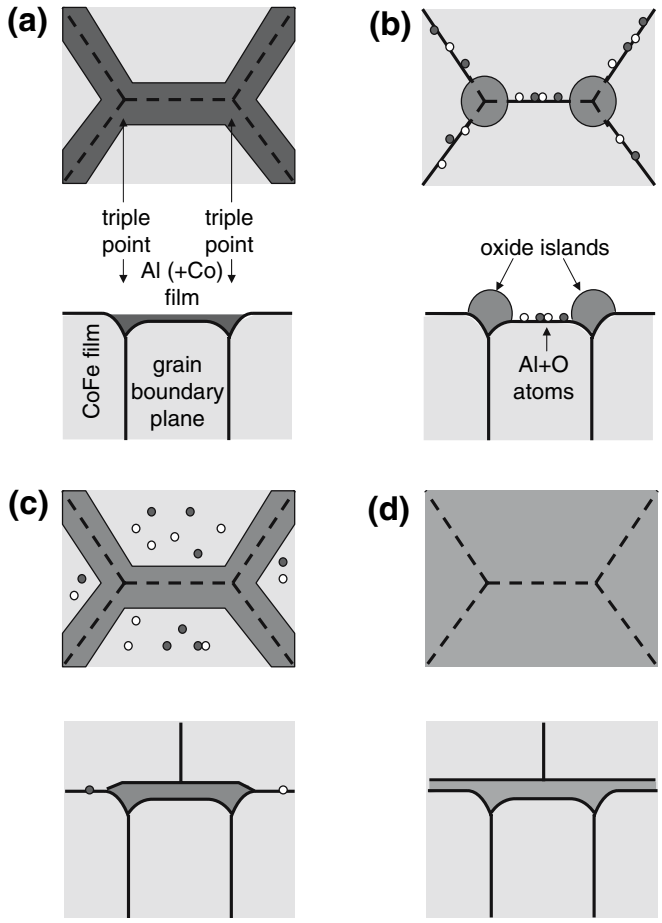

Fig. 4 Schematic diagram showing the different morphologies observed for the oxide barrier in the MTJ structure after the various stages in the fabrication process: (**a**) Al layer deposition, (**b**) partial oxidation, (**c**) full oxidation and capping; and (**d**) annealing. Top row shows plan views from the barrier plane downwards, while the bottom row shows cross-sectional views through the centre of the structure (cutting though a grain boundary)

show that it forms a continuous layer [24]. Calculations of Al deposition on a $Co_{90}Fe_{10}$ substrate give similar results [25]. This is to be expected, given the lower surface energy of Al, as is shown quantitatively by Zhou and Wadley [24]. However, these simulations were performed assuming a relatively flat substrate. The underlying CoFe layer in the experimental structures shows a high degree of [111] crystallographic texture and considerable grain boundary grooving leading to a rough, wavy surface onto which the Al is deposited (Fig. 1a). Given the low surface energy of Al, it is likely to act in a similar way to Cu deposited onto CoFe and smooth any correlated roughness in the underlying layer [26]. However, the limited thickness of the Al deposited will not be sufficient to fill in the 'grooves' at the grain boundaries in the underlying layer, and is therefore likely to only partially cover the surface, Fig. 4a.

It has been shown that depositing Al onto Co produces an intermixed region about 1 nm wide [27, 28]. (The difference in Al and Co surface energies mean that the intermixing when Co is deposited on Al is even greater.) This is consistent with the high degree of solubility of up to 15 at.% Al in fcc Co–Fe [29], and the formation of a CoAl intermetallic phase over of broad range of compositions [30]. Although neither of these are exactly what we observe in the 3DAP, they indicate that the energy of intermixing of Co and Al is low, and so it is not surprising that intermixing occurs during a low temperature, non-equilibrium growth, technique such as sputtering. (The intermixing was not predicted by the simulations of Zhou and Wadley, probably because they used very low simulated Al ion energies during this stage of the process.) Therefore, the nominally 0.6 nm Al deposited in the present structures would be expected to form a intermixed Al + Co fcc layer, probably showing less correlated roughness on the top surface than at the lower interface.

Oxidation of the Al (+ Co) layer proceeds via the formation of an oxide which not only retains a high level of Co, but also contains much less oxygen than would be expected given the stable Al_2O_3 stoichiometry. This may be considered surprising: whereas the native oxide in silicon is usually termed SiO_x, few references use similar terminology for the low temperature oxide of aluminium. Indeed, the high heat of formation would lead to the assumption that the stable stoichiometry is formed immediately. However, in the case of oxidation of the barrier layers, the supply of oxygen is limited and this, together with the presence of substantial quantities of Co, is likely to prevent the formation of the stable oxide composition. Thus, it is common in the field of MTJ structures formed by low pressure, low temperature oxidation to refer to AlO_x barriers. It should be noted that CoO and Al_2O_3 form a mixed oxide [31], and although this is clearly not what is present here, it makes it less surprising that a significant level of Co remains present within the barrier of these highly metastable structures, even after annealing.

Using molecular dynamics calculations, Zhou and Wadley simulate the oxidation of an Al layer on a $Ni_{65}Co_{20}Fe_{15}$ substrate, and show that for layers of 0.6 nm or less, the layer de-wets under oxidation to form isolated oxide islands [24]. Thus, even if our initial Al(+ Co) layer does form a continuous layer, it is expected that the oxidation will result in the formation of islands. Simulating oxidation on an Al layer with some degree of roughness, the thinner regions of the Al layer are the first to de-wet, with the oxide islands forming at positions where the initial Al layer was the thickest [24]. This de-wetting is driven by the surface energy change, since the Al surface energy is low but both the Al oxide surface energy and the metal/oxide interface energy are high. Zhou and Wadley calculate a wetting angle of $\cos^{-1}(-0.56) = 124°$, although their calculated surface energies are somewhat high: for example they calculate a Al_2O_3 surface energy of 0.341 eV/Å^2 (5.5 J m^{-2}). Despite this, and despite the fact that their calculations are for pure Al oxide rather than for a mixed Co–Al oxide, a wetting angle of around 90° would be reasonable. Our 3DAP results are consistent with the view that the oxide is in the form of islands on the surface of the CoFe, although in the presence of correlated roughness the initial film may not be continuous. The oxide would form at the initial position of the metal, at grain boundaries and triple points in the underlying CoFe layer, Fig. 4b and c. Should a continuous metal film be present initially, it would still be thicker in these regions. Thus the initial stages of oxidation would again result in isolated islands located at the triple points, Fig. 4b where the Al (+ Co) layer is thickest. Further oxidation, which will increase the volume of the oxide layer, allows it to wet the grain boundary groove formed by the correlated roughness, Fig. 4c, thus forming a network on the surface of the CoFe before it is capped by further CoFe deposition. A similar process occurs in the under-oxidised material on annealing, with additional driving force provided by the consumption of Al and O that appears to penetrate a small distance into the grain boundary region, and is observed between the islands.

On annealing the fully oxidised sample, the network of oxide that delineates the grain boundaries is seen to 'heal' to form a continuous layer. This involves the creation of a significant amount of metal/oxide

interface, and so appears to be energetically unfavourable. There will however be a number of factors that may reduce the overall energy cost of creating the extra metal/oxide interface. Given the contamination of the underlying CoFe, first by the Al deposition and then by oxidation, it is likely that subsequent growth of the top CoFe layer will not be epitaxial, even between the oxide islands that have formed, though the (111) texture will largely be maintained by the lower energy of the Co[111] surface. Thus, the original CoFe surface will become a twist grain boundary, contributing some interface energy to the as-deposited state which will be recovered when the continuous oxide layer is formed following annealing. However, this effect is likely to be only a small contribution: the grain boundary energy is likely to be around 0.7 J m^{-2} [32] relative to a CoFe/Al_2O_3 interface energy, which is not much lower that the Al_2O_3 surface energy, which has been estimated at around 1.7 J m^{-2} for γ alumina [33]. (The 'quasi-amorphous' γ-alumina surface energy is used here, as opposed to that for α-alumina [34], since the amorphous barrier layers are considered to be closer to the former structure. For example, atomic spacings measured from radial distribution functions of such layers are found to be closer to that in γ-alumina [35]. Amorphous alumina is also seen to crystallise to γ-alumina rather than α-alumina [36]). Of course, it should be taken into account that the oxide is not Al_2O_3 but contains a significant amount of Co, and this is likely to reduce the oxide/metal surface energy. Nonetheless, it is would not be reasonable to expect the interface energy between the amorphous oxide and the crystalline metal to be half of the CoFe grain boundary energy, which would be required for wetting. Another factor is the presence of aluminium and oxygen at the grain boundaries in the underlying CoFe layer, which will release energy as the oxide forms a continuous layer and incorporates those atoms. This is potentially a very significant contribution. Taking the measured oxygen coverage of 6.2×10^{18} atoms/m^2 in the region between the islands in the as-deposited unannealed film, and a formation energy for Al_2O_3 of 1690 kJ/mol [37], complete reaction of these O atoms with pure Al would generate about 5.8 J m^{-2} in reacting with Al. However, it is not clear how much of this energy would be available. Not only is the oxide already partially reacted, so that the heat of formation to complete the reaction is likely to be lower, but the O is present with Al and likely to be bound to it, and to the CoFe. For example, the heat of formation of CoO is nearly 239 kJ/mol [37], which is over 40% of that for Al_2O_3 per mole of oxygen, meaning that less energy is available for the completion of aluminium oxidation. In addition, the Al:O ratio for the regions between the barrier is approximately 4:3, very similar to that for the barrier, so it is not clear that incorporation of this material would provide the necessary driving force for the oxide to form a continuous layer.

There are however other factors that could come into play to drive the oxide to form a continuous layer. One possible mechanism is the healing of holes in an oxide which is observed by Zhou et al. during the simulation of oxidation of Al on a $Ni_{65}Co_{20}Fe_{15}$ substrate [38]. In these simulations, transient holes are found to open in the growing oxide as the initial stage of de-wetting, but these then self-heal as the oxide layer becomes thicker. The driving force for the healing of these holes is the surface energy of the side-wall of the hole: as the film becomes thicker, this energy term becomes larger and it becomes energetically favourable for the hole to close. Although these simulations were carried out for the case of a growing oxide film with a free upper surface, a simple model can be used to illustrate this further for an encapsulated film. Assume an oxide layer of thickness h encapsulated in metal, such that the metal/oxide interface energy is γ, in which there is a cylindrical hole of radius r. The change in energy of the system in forming the hole is given by the interface energy of the edge of the hole, less the interface energy of the layer that has been removed

$$\Delta E = 2\pi rh\gamma - 2\pi r^2\gamma \quad (1)$$

As shown in Fig. 5, the change of energy is positive for small hole sizes, but negative for large holes: the equilibrium state is for the layer to break up but if a sufficiently small hole forms, it will self-heal. The

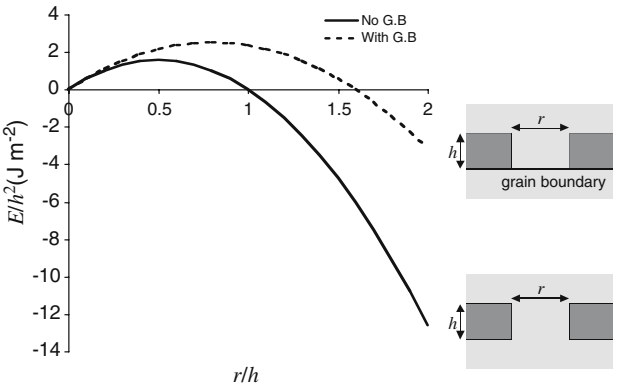

Fig. 5 Change in energy resulting from the formation of a hole of radius r in a layer of thickness h. Solid line shows the case of $\gamma = 1$ J m^{-2} in the absence of a grain boundary. Dashed line shows the case where the layer is on a grain boundary of energy $\gamma_{gb} = 0.75$ J m^{-2}

critical hole size, below which holes will not grow, is easily calculated to be $h/2$. Therefore, for our oxide layer with a thickness of about 1 nm, this mechanism would only close holes of 1 nm diameter or less and does not explain the closure of holes nearly 10 nm in diameter. Of course, this calculation makes a number of major simplifications: in particular it assumes that the metal/oxide interface energy is the same for the top and bottom of the layer and at the edge of the hole. This seems a reasonable assumption for an interface between a metal and an amorphous oxide, but does not take into account the presence of the twist grain boundary in the hole, between the upper and lower metal layers, or of oxygen trapped in the lower CoFe layer and at the in-plane CoFe grain boundary, as described above. These would effectively reduce the energy of the lower metal/oxide interface. If we assume that the oxide is on a grain boundary with an effective interface energy of γ_{gb} (including the effects of trapped oxygen), the energy of the hole is modified from that given in Eq. 1 and is now

$$\Delta E = 2\pi rh\gamma - \pi r^2\left(2\gamma - \gamma_{gb}\right) \tag{2}$$

which gives an increase of the critical hole size by a factor of $2\gamma/(2\gamma - \gamma_{gb})$ over the simple model. Figure 5 shows the results of this equation for the case of $\gamma = 1$ J m^{-2} and $\gamma_{gb} = 0.75$ J m^{-2}, which still only predicts healing to occur for holes smaller than 1.6 nm in diameter, and is not sufficient to explain the hole healing observed in the experiments. Both previous expressions assume a square-edged hole, which is energetically unrealistic, but a more realistic rounded profile would decrease the surface area and thus the energy contribution from the hole. This would therefore have the effect of reducing the critical hole size.

It must also be realised that the barrier layer is not a closed system but, through gettering oxygen from the rest of the film, the oxide is growing during the annealing process. During this growth, strain energy will be generated in the matrix by the expansion of the oxide, as it converts from a Al:O ratio of approximately 2:1 to the stoichiometric ratio of 2:3. The overall expansion between Al and Al_2O_3 is about 30%, which although smaller than the volume expansion of 150% on oxidation of Si, is nonetheless significant. Nabarro gives the matrix strain energy per unit volume of an ellipsoidal incompressible particle as

$$\Delta E_S = {}^2/_3\mu(\Delta V)^2 f(c/a) \tag{3}$$

where ΔV is the relative change in volume, μ is the shear modulus for the matrix, and $f(c/a)$ is a function that takes into account the shape of the particle, being 1 for a sphere, $^3/_4$ for a needle and 0 for an infinitely thin disk [39]. Thus, in the presence of significant strain energy, the energy can be reduced by a shape change of the particle, and this will compensate to some degree for the increase in the surface energy. In the case where the particle is compressible, the equation for the strain above is modified by a factor of

$$\frac{3\kappa p}{(3\kappa p + 4\mu)} \tag{4}$$

where κ_p is the bulk modulus of the particle. The factor in Eq. 4 tends to 1 in the case where $\kappa_p >> \mu$ [40]. Taking standard values of $\kappa_p = 165$ GPa and $\mu = 75$ GPa gives a factor of 0.625.

The effect of this strain term on the energetics of the particle is shown in Fig. 6 for the case of a ellipsoidal particle of constant volume, equivalent to a 2 nm radius spherical particle, with a surface energy of 1 J m^{-2}. Two of the ellipsoid radii (a, b) are kept equal, and these are in the plane of a grain boundary of energy 0.75 J m^{-2}, this energy being released if the particle grows across the plane of the boundary. The third radius, c, is normal to this plane, and is allowed to

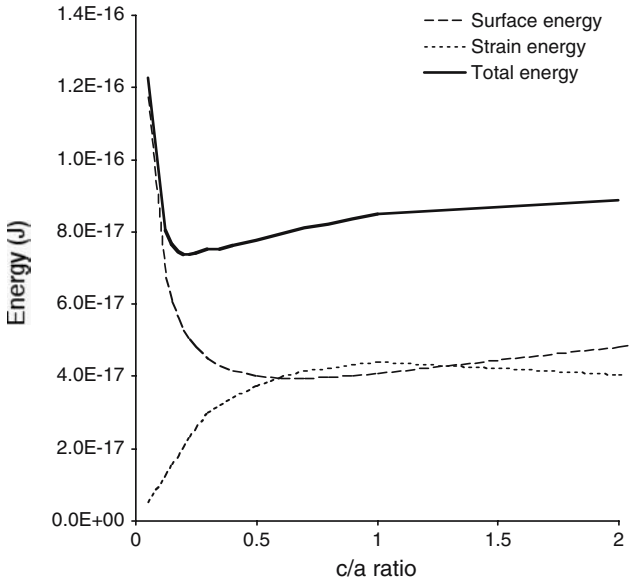

Fig. 6 Surface and strain contributions to the total energy of a confined ellipsoidal particle that undergoes a volume expansion of 20%, as a function of the c/a ratio. The particle is taken to have an interface energy of $\gamma = 1$ J m^{-2} and be sited on a grain boundary of energy $\gamma_{gb} = 0.75$ J m^{-2}

vary such that the particle changes from a thin flat plate ($c/a < 1$) to an elongated rod ($c/a > 1$). The presence of the grain boundary biases the surface energy term, making a plate-shaped particle the preferred shape in the absence of strain. However, this is only a limited effect, the minimum in the surface energy occuring for $c/a = 0.7$. Reduction of strain energy for the plate-shaped particle has a significant effect, producing a minimum in the total energy at a c/a ratio of around 0.2, where the plate thickness is a little over 1 nm and the diameter is close to 7 nm. While this diameter is smaller that the average grain size, it suggests that this effect would be sufficient to spread out the oxide to a level where the hole healing effect would start to play a part, closing the final pinhole and forming a continuous layer.

Although not producing a single unified analytical description for the energetics of the network of oxide islands closing to form a continuous layer, the discussion above strongly suggests that sufficient driving force for the process does exist. Even neglecting the possible effects of the oxygen trapped at the grain boundary between the islands, by taking into account the presence of a grain boundary at the original surface, the effect of strain and the closure of pinholes due to the energy of the edge of the hole, the spreading of the oxide to form a continuous layer can be shown to be energetically favourable for realistic values of the metal/oxide interface energy (1 J m^{-2}). However, this metal/oxide interface energy only seems plausible because of the presence of a substantial amount of Co in the oxide, which produces a graded interface and reduces the interface energy from the value that would be expected in the case of a Co/Al_2O_3 interface. Indeed, the observation that the oxygen extends further vertically across the barrier than the aluminium (especially into the lower Co layer) suggests there is more of a core-shell structure to the oxide after annealing, the core being Al-rich and the shell being richer in Co. This may be formed naturally as the Co from the centre of the barrier is rejected to bring the oxide composition closer to Al_2O_3. However, the result would be that the Co-enriched shell would produce a lower interface energy.

Acknowledgements The authors are grateful to Prof. G.D.W. Smith FRS for provision of laboratory facilities and for helpful discussions during the preparation of this paper. We would also like to thank Xiaowang Zhou, University of Virginia, for valuable contributions on the mechanisms of oxide growth. Laser-pulsed 3DAP experiments were performed at Oxford nanoScience Limited, Milton Keynes, UK and we are grateful to Dr. Peter Clifton for his assistance in the collection of the data. This work was supported by funding from the Engineering and Physical Sciences Research Council. AC is also grateful for support from Oxford nanoScience Limited during the writing of this paper. Argonne National Laboratory is supported by the U.S. Department of Energy, Basic Energy Sciences – Materials Sciences, under contract (W-31-109-ENG-38.

References

1. Barthélémy A, Fert A, Contour J-P, Bowen M, Cros V, de Teresa JM, Hamzic A, Faini JC, George JM, Grollier J, Montaigne F, Pailloux F, Petroff F, Vouille C (2002) J Mag Mag Mat 242–245:68
2. Jullière M (1975) Phys Lett 54A:225
3. Moodera JS, Kinder LR, Wong TM, Meservey R (1995) Phys Rev Lett 74:3273
4. Moodera JS, Kinder LR, Nowak J, Leclair P, Meservey R (1996) Appl Phys Lett 69:708
5. Moodera JS, Kinder LR (1996) J Appl Phys 79:4724
6. Park BG, Lee TD, Lee TH, Kim CG, Kim CO (2003) J Appl Phys 93:6423
7. Bae JS, Shin KH, Lee HM (2002) J Appl Phys 91:7947
8. Tsymbal EY, Mryasov ON, Le Clair PR (2003) J Phys Condens Matt 15:R109
9. Tsymbal EY, Pettifor DG (1998) Phys Rev B 58:432
10. Da Costa V, Tiusan C, Dimopoulos T, Ounadjela K (2000) Phys Rev Lett 85:876
11. Rabson DA, Jönsson-Åkerman BJ, Romero AH, Escudero R, Leighton C, Kim S, Schuller IK (2001) J Appl Phys 89:2786
12. Shang P, Petford-Long AK, Nickel JH, Sharma M, Anthony TC (2001) J Appl Phys 89:6874
13. Ozkaya D, Mcbride W, Cockayne DJH (2004) Interface Sci 12:321
14. Ozkaya D, Dunin-Borkowski RE, Petford-Long AK, Wong PK, Blamire MG (2000) J Appl Phys 87:5200
15. Stobiecki T, Kanak J, Wrona J, Czapkiewicz M, Kim CG, Kim CO, Tsunoda M, Takahashi M (2004) Phys Stat Sol A 201:1621
16. Zhu W, Hirschmugl CJ, Laine AD, Sinkovic B, Parkin SSP (2001) Appl Phys Lett 78:3103
17. Miller MK, Cerezo A, Hetherington MG, Smith GDW (1996) Atom probe field ion microscopy. Oxford University Press, Oxford
18. Cerezo A, Larson DJ, Smith GDW (2001) MRS Bull 26:102
19. Petford-Long AK, Ma YQ, Cerezo A, Larson DJ, Singleton EW, Carr BW (2005) J Appl Phys 98:124904
20. Larson DJ, Wissman BD, Martens RL, Viellieux RJ, Kelly TF, Gribb TT, Erskine HF, Tabat N (2001) Micro Microanal 7:24
21. Larson DJ, Petford-Long AK, Ma YQ, Cerezo A (2004) Acta Mater 52:2847
22. Cerezo A, Godfrey TJ, Sibrandij SJ, Smith GDW, Warren PJ (1998) Rev Sci Instrum 69:49
23. Lehnert T, Billon D, Grassl C, Grundlach KH (1992) J Appl Phys 72:3165
24. Zhou XW, Wadley HNG (2005) Phys Rev B 71:054418
25. Zhou XW, Wadley HNG, private communication
26. Larson DJ, Cerezo A, Clifton PH, Petford-Long AK, Martens RL, Kelly TF, Tabat N (2001) J Appl Phys 89:7517
27. Gas P, Bergman C, Lábár JL, Barna PB, D'heurle FM (2004) Appl Phys Lett 84:2421
28. Buchanan JDR, Hase TPA, Tanner BK, Chen PJ, Gan L, Powell CJ, Egelhoff WF Jr (2003) J Appl Phys 93:8044
29. Raynor GV, Rivlin VG (1988) Phase equilibria in iron ternary alloys. Institute of Materials, London, p 76

30. Macallister AJ (1990) In: Massalski TB, Okamoto H, Subramaniam PR, Kacprzak L (eds) Binary alloy phase diagrams, 2nd edn. ASM International, OH, p 136
31. Levin EM, Mcmurdie HF (1975) Phase diagrams for ceramicists, 1975 supplement. American Ceramic Society, Columbus, OH, pp 236
32. Murr LE (1975) Interfacial phenomena in metals and alloys. Addison-Wesley, London
33. Mchale JM, Auroux A, Perotta AJ, Navrotsky A (1997) Science 277:788
34. Levi G, Kaplan WD (1997) Acta Mater 51:788
35. Ozkaya D, Mcbride W, Cockayne DJH (2004) Interface Sci 12:321
36. Fei GT, Barnes JP, Petford-Long AK, Doole RC, Serna R, Gonzalo J (2002) J Phys D Appl Phys 35:916
37. Weast RC (1983) CRC handbook of chemistry and physics, 63rd edn. CRC Press, Boca Raton, FL
38. Zhou XW, Wadley HNG, Wang DX, submitted to Comput Mater Sci
39. Nabarro FRN (1940) Proc Roy Soc A 175:519
40. Christian JW (2002) The theory of transformations in metals and alloys, Part I. 2nd edn. Elsevier, pp 464